PHYSICAL REVIEW A **83**, 043820 (2011)

Local-field correction in the strong-coupling regime

Tran Minh Hien,[1] Ho Trung Dung,[1] and Dirk-Gunnar Welsch[2]
[1]*Institute of Physics, Academy of Sciences and Technology, 1 Mac Dinh Chi Street, District 1, Ho Chi Minh City, Vietnam*
[2]*Theoretisch-Physikalisches Institut, Friedrich-Schiller-Universität Jena, Max-Wien-Platz 1, D-07743 Jena, Germany*

(Received 9 January 2011; published 18 April 2011)

The influence of the local-field correction on the strong atom-field coupling regime are investigated using the real-cavity model. The atom is positioned at the center of a multilayer sphere. Three types of mirrors are considered: perfectly reflecting, Lorentz band gap, and Bragg-distributed ones, with special emphasis on experimental practicability. In particular, the influence of the local field on the spectral resonance lines, the Rabi oscillation frequency and decay rate, and the condition indicating the occurrence of the strong-coupling regime are studied in detail. It is shown that the local-field correction gives rise to a structureless plateau in the density of states of the electromagnetic field. The level of the plateau rises with increasing material density and/or absorption, which may eventually destroy the strong-coupling regime. The effect of the local field is especially pronounced at high-material densities due to direct energy transfer from the guest atom to the medium. At lower material density and/or absorption, variation of the material density does not seem to affect much the strong-coupling regime, except for a small shift in the resonance frequency.

DOI: 10.1103/PhysRevA.83.043820　　PACS number(s): 42.50.Ct, 42.50.Nn, 12.20.Ds

I. INTRODUCTION

For a long time it has been known that when a guest atom is embedded in a host medium then the electromagnetic field acting on it differs in general from the macroscopic field obtained by performing an unweighted spatial average over an appropriately chosen unit cell [1,2]. This leads to the need to locally correct the field. In quantum optics the problem of local-field correction has been typically studied in conjunction with the problem of spontaneous decay of an excited guest atom. Microscopic theories have been developed, for example, for crystals [3,4] and disordered dielectrics [5–8]. In macroscopic approaches to the problem, local-field effects have been taken into account by regarding the guest atom as being enclosed in a sufficiently small virtual [1,9] or real (spherical) cavity [2,10–14]. In the virtual-cavity model the cavity is regarded as being part of the host medium. In the real-cavity model, on the contrary, the cavity is assumed to be empty so that the guest atom is situated in a free-space region between the host atoms, with the cavity radius being a measure of the average distance from the guest atom to the medium constituents. Microscopic models often agree with the virtual-cavity results [3,5,6,8], while recent experiments on spontaneous emission of atoms embedded in dielectrics support the real-cavity model [15–18]. It has been presumed that while the virtual-cavity model may apply to interstitial atoms, the real-cavity model may be specific to substitutional atoms, the case of substitutional atoms occurring prevalently for impurity atoms in disordered dielectrics [4].

As known, spontaneous emission is caused by resonant interaction of an excited atom with a typically continuous radiation field. If the spectral width of the field in the neighborhood of the atomic transition frequency considered is much larger than the atom-field coupling strength expressed in terms of the Rabi frequency, the spontaneous decay can be regarded as being an irreversible process, and the atom and the field are said to be in the weak-coupling regime. When, on the other hand, the spectral width of the radiation is sufficiently small so that effectively an almost single-mode field interacts with the atomic transition, then the energy initially stored in the excited atom will bounce back and forth between the two systems, which in this case are said to be in the strong-coupling regime.

In previous treatments of local-field effects in spontaneous emission, the host medium is typically assumed to be a bulk medium that extends homogeneously to infinity, and the atom-field interaction is in the weak-coupling regime. The effect of finite size and shape of the host medium on the local field for weak atom-field coupling has been considered recently [12,19]. In this regime the dynamics of the atomic upper-level population just follows an exponential decaying law. A more interesting behavior appears in the strong-coupling regime, which manifests itself in vacuum Rabi oscillations of the atomic inversion and in the vacuum Rabi splitting of the spontaneous emission spectrum. Due to recent developments in quantum cavity electrodynamics where high-quality resonators are fabricated and applications in light-emitting devices and quantum information processing are envisaged, the need to evaluate the local-field correction in the strong-coupling regime becomes actual from the viewpoint of both fundamental research and practical applications.

To study the effect of local-field correction on the atom-field interaction in the strong-coupling regime, we consider a system consisting of a two-level atom embedded at the center of a sphere made of a nonmagnetic material of permittivity $\epsilon(\omega)$. The sphere is coated by a highly reflecting mirror which confines the electromagnetic field in all three dimensions guaranteeing that conditions for the strong-coupling regime can be met. Three types of mirror made from purely electrically responding matter will be considered: a perfectly reflecting mirror, a Lorentz band-gap mirror, and a Bragg-distributed mirror [20,21]. Local-field effects are described by assuming a real cavity surrounding the guest atom. The radius of the cavity R_C is typically much smaller than the characteristic wavelength in the system, in which case the local-field effects become significant. The fact that the Green tensor of concentric spheres is known in closed form [20–22] makes this system well suited for an investigation of the effect of local-field correction on the atom-field interaction in the strong-coupling regime. Bragg-distributed dielectric microspheres can now be fabricated in laboratories using, for example, a combination of etching and chemical-vapor deposition [23], multistage emulsion polymerization [24], or thermal printing [25], meaning that the system under consideration is within the reach of today's experimental techniques.

The appearance of Rabi oscillations of the upper-level population of the two-level atom, which is assumed to be initially prepared in the upper state, can be regarded as an evidence for the strong-coupling regime. The strength of the local-field correction can be manipulated by varying the radius of the real cavity, which, as already mentioned, represents the average distance from the guest atom to the neighboring constituents of the material, and by tuning the degree of material absorption. Effects of the local-field correction on the Rabi frequency, the Rabi-oscillations damping rate, and the conditions under which the strong-coupling regime can occur, will be discussed.

The paper is organized as follows. Basic formulas necessary for the calculation of the Rabi frequency and damping rate are summarized in Sec. II. The local-field corrections in the case of a perfect mirror, a Lorentz band-gap mirror, and a Bragg-distributed mirror are investigated in Secs. III, IV, and V, respectively. Conclusions are made in Sec. VI.

II. BASIC FORMULAS

The calculations are based on the quantization scheme for the electromagnetic field in purely electrically responding media [26,27], which leave the magnetic field unaffected, and has been used to describe the atom-field interaction in the presence of such media [28]. Let us consider a neutral two-level atom (position $\mathbf{r}_\mathrm{A}$, transition frequency ω_A) that resonantly interacts with the medium-assisted electromagnetic field via an electric-dipole transition (dipole moment $\mathbf{d}_A$). The atom is initially prepared in the excited state while the medium-assisted field is initially in the ground state, that is, the medium-assisted vacuum state. A resonator usually can support multiple resonance lines. When the atomic transition frequency ω_A approaches a resonance frequency ω_m, contributions from other resonances can be neglected. Suppose the density of the medium-assisted field states is a Lorentzian centered around ω_m, with half width at half maximum $\delta\omega_m$, then the amplitude $C_u(t)$ of the overall-system state where the atom is excited and the field is in the vacuum state satisfies [28]

$$\ddot{C}_u(t) + [i(\omega_m - \omega_\mathrm{A}) + \delta\omega_m]\,\dot{C}_u(t) + (\Omega/2)^2 C_u(t) = 0, \quad (1)$$

where

$$\Omega = \sqrt{2A(\omega_m)\delta\omega_m} \quad (2)$$

is the Rabi frequency,

$$A(\omega) = \frac{2\omega^2}{\hbar\epsilon_0 c^2}\mathbf{d}_\mathrm{A}\mathrm{Im}\,\boldsymbol{G}(\mathbf{r}_\mathrm{A},\mathbf{r}_\mathrm{A},\omega)\mathbf{d}_\mathrm{A} \quad (3)$$

gives us a measure of the density of field states, $\boldsymbol{G}(\mathbf{r},\mathbf{r}',\omega)$ is the Green tensor describing the medium surrounding the guest atom, and the electric-dipole and rotating wave approximations have been employed.

Equation (1) is obviously an equation of motion of a damped oscillator. When $\omega_A = \omega_m$ and

$$\frac{\Omega}{\delta\omega_m} = \sqrt{\frac{2A(\omega_m)}{\delta\omega_m}} \gg 1, \quad (4)$$

then damped Rabi oscillations are observed, with $\delta\omega_m$ being the damping rate,

$$|C_u(t)|^2 = e^{-\delta\omega_m t}\cos^2(\Omega t/2), \quad (5)$$

and we are in the so-called strong-coupling regime. The inequality (4) is an indicator of whether the strong-coupling regime is realized or not. In the opposite limit when $\Omega \ll \delta\omega_m$, then an overdamped or purely decaying behavior is observed $|C_u(t)|^2 = e^{-A(\omega_m)t}$, and we are in the weak-coupling regime, in which $A(\omega_m)$ has the physical meaning of the spontaneous decay rate. The Rabi frequency (2), the damping rate $\delta\omega_m$, and the strong-coupling condition (4) depend on the Green tensor, and therefore, on all changes when we vary the size of the cavity or exclude it altogether.

For all three types of resonators under consideration, the resonator, including the cavity surrounding the atom, is considered to be a sphere consisting of L concentric layers, each having permittivity $\epsilon_i(\omega)$, i running from 1 to L starting from the outermost layer. The spherical surfaces have radii R_j $(j = 1,2,\ldots,L-1)$ [see Fig. 1]. The Green tensor at equal positions can be decomposed into a bulk part, which is the vacuum part in our case, and a reflection part,

$$\boldsymbol{G}(\mathbf{r}_A,\mathbf{r}_A,\omega) = \boldsymbol{G}^\mathrm{V}(\mathbf{r}_A,\mathbf{r}_A,\omega) + \boldsymbol{G}^\mathrm{R}(\mathbf{r}_A,\mathbf{r}_A,\omega). \quad (6)$$

For a multilayer sphere and $\mathbf{r}_A = 0$, after some algebra it can be found that [28]

$$\boldsymbol{G}^\mathrm{R}(\mathbf{r}_A,\mathbf{r}_A,\omega)\Big|_{\mathbf{r}_A\to 0} = \frac{i\omega}{6\pi c}C_N^{LL}(\omega)\boldsymbol{I} \quad (7)$$

($\boldsymbol{I}$ is the unit tensor). The index N indicates contributions of the TM waves to be distinguished from those of the TE waves. As can be seen from above, only TM waves are involved, which is a consequence of the fact that the atom is located at the sphere center. Substitution of Eq. (7) into Eq. (3) yields

$$\bar{A}(\omega) = 1 + \mathrm{Re}\,C_N^{LL}(\omega), \quad (8)$$

where $\bar{A}(\omega) \equiv A(\omega)/A_0$, $A_0 = k_\mathrm{A}^3 d_\mathrm{A}^2/(3\hbar\pi\epsilon_0)$ is the spontaneous decay rate in free space ($k_\mathrm{A} = \omega_\mathrm{A}/c$),

$$C_N^{LL} = \frac{\mathcal{T}_{21}}{\mathcal{T}_{11}}, \quad (9)$$

and $\mathcal{T}$ is a 2×2 matrix defined as

$$\mathcal{T} = \mathbf{T}_N^{L-1}\mathbf{T}_N^{L-2}\cdots\mathbf{T}_N^{1}, \quad (10)$$

$$\mathbf{T}_N^f = \begin{bmatrix} \frac{1}{T_{Ff}^N} & \frac{R_{Ff}^N}{T_{Ff}^N} \\ \frac{R_{Pf}^N}{T_{Pf}^N} & \frac{1}{T_{Pf}^N} \end{bmatrix}. \quad (11)$$

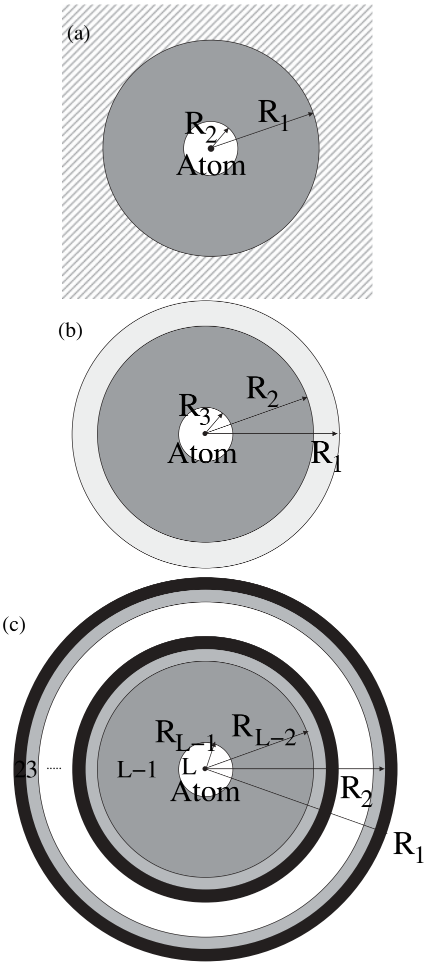

FIG. 1. Schematics of the resonators with a (a) perfectly reflecting mirror, (b) Lorentz band-gap mirror, and (c) Bragg-distributed mirror.

The symbols $T^N_{(P,F)f}$ and $R^N_{(P,F)f}$ represent the centripetal and centrifugal transmission and reflection contributions,

$$\begin{aligned}
R^N_{Pf} &= \frac{k_{f+1} H_{(f+1)f} H'_{ff} - k_f H_{ff} H'_{(f+1)f}}{k_{f+1} J'_{ff} H_{(f+1)f} - k_f J_{ff} H'_{(f+1)f}},\\
R^N_{Ff} &= \frac{k_{f+1} J_{(f+1)f} J'_{ff} - k_f J_{ff} J'_{(f+1)f}}{k_{f+1} J_{(f+1)f} H'_{ff} - k_f J'_{(f+1)f} H_{ff}},\\
T^N_{Pf} &= \frac{k_{f+1}\left(J'_{(f+1)f} H_{(f+1)f} - J_{(f+1)f} H'_{(f+1)f}\right)}{k_{f+1} J'_{ff} H_{(f+1)f} - k_f J_{ff} H'_{(f+1)f}},\\
T^N_{Ff} &= \frac{k_{f+1}\left(J_{(f+1)f} H'_{(f+1)f} - J'_{(f+1)f} H_{(f+1)f}\right)}{k_{f+1} J_{(f+1)f} H'_{ff} - k_f J'_{(f+1)f} H_{ff}},
\end{aligned} \tag{12}$$

where

$$J_{il} = j_n(z_{il}), \qquad Y_{il} = y_n(z_{il}), \tag{13}$$

$$H_{il} = h^{(1)}_n(z_{il}) = j_n(z_{il}) + i y_n(z_{il}), \tag{14}$$

$$J'_{il} = \frac{1}{z}\frac{d[z j_n(z)]}{dz}\bigg|_{z=z_{il}}, \qquad Y'_{il} = \frac{1}{z}\frac{d[z y_n(z)]}{dz}\bigg|_{z=z_{il}}, \tag{15}$$

$$H'_{il} = \frac{1}{z}\frac{d[z h^{(1)}_n(z)]}{dz}\bigg|_{z=z_{il}} = J'_{il} + i Y'_{il}, \tag{16}$$

with $z_{il} = k_i R_l$, $k_i = \sqrt{\epsilon_i(\omega)}\,\frac{\omega}{c}$, $j_n(z)$ [$y_n(z)$] being the first-kind [second-kind] spherical Bessel functions, and $h^{(1)}_n(z)$ being the first-kind spherical Hankel function. The Green tensor contains, in general, sums over n. Note that due to the fact that the atom is put at the sphere center, only spherical functions of order $n = 1$ contribute [28].

Clearly local-field corrections will be noticeable only when the medium is sufficiently dense. In our model this means that the radius of the cavity should be much smaller than the atomic transition wavelength

$$k_{\mathrm{A}} R_C \ll 1. \tag{17}$$

Under this condition it was conjectured in Ref. [12] and later proved in Ref. [19] for an arbitrary geometry of the material body surrounding the guest atom that the Green tensor can be decomposed as

$$\begin{aligned}
\boldsymbol{G}^R(\mathbf{r}_{\mathrm{A}},\mathbf{r}_{\mathrm{A}},\omega_{\mathrm{A}}) &= \frac{k_{\mathrm{A}}}{6\pi}\left\{\frac{3(\epsilon-1)}{2\epsilon+1}\,\frac{1}{(k_{\mathrm{A}} R_{\mathrm{C}})^3}\right.\\
&\quad \left. + \frac{9(\epsilon-1)(4\epsilon+1)}{5(2\epsilon+1)^2}\,\frac{1}{k_{\mathrm{A}} R_{\mathrm{C}}} + i\left[\frac{9\epsilon^{5/2}}{(2\epsilon+1)^2} - 1\right]\right\}\boldsymbol{I}\\
&\quad + \left(\frac{3\epsilon}{2\epsilon+1}\right)^2 \boldsymbol{G}^R_{\mathrm{B}}(\mathbf{r}_{\mathrm{A}},\mathbf{r}_{\mathrm{A}},\omega_{\mathrm{A}}) + O(k_{\mathrm{A}} R_{\mathrm{C}}),
\end{aligned} \tag{18}$$

where $\epsilon \equiv \epsilon(\omega_A)$ denotes the permittivity of the medium in which the guest atom is embedded and $\boldsymbol{G}^R_{\mathrm{B}}$ is the scattering part of the Green tensor without the cavity. This decomposition is not only helpful in the study of the local-field correction in the weak-coupling regime [19], but, as we shall see below, it also proves to be insightful in the strong-coupling regime.

We now can proceed to distinguish various types of mirrors. In particular, $R_C = R_2$, $\epsilon = \epsilon_2$ in the perfectly reflecting mirror model, $R_C = R_3$, $\epsilon = \epsilon_3$ in the Lorentz band-gap mirror model, and $R_C = R_{L-1}$, $\epsilon = \epsilon_{L-1}$ in the Bragg reflecting mirror model (Fig. 1). If R_w denotes the radius of the inner resonator wall, it is equal to R_1, R_2, and R_{L-2} in the three respective models.

III. PERFECTLY REFLECTING MIRROR

The aim of this section is twofold. First we make use of the small-cavity expansion (18) and second we elucidate its domain of validity in the strong-coupling regime (for its applicability in the weak-coupling regime see Ref. [19]). Recall that the resonator consists of three layers, the innermost one being the cavity in the real-cavity model [Fig. 1(a)]. To simulate the perfectly reflecting mirror we let the permittivity of the outermost layer be real and tend to infinity, $\epsilon_1 \to \infty$. Then $R^N_{P1} \to \frac{H_{11}}{J_{11}}$ [29] and

$$\begin{aligned}
C^{33}_N &= \frac{T^N_{F2}}{T^N_{P2}}\left(\frac{J'_{21} H_{11} R^N_{P2} - J_{11} H'_{21} R^N_{P1}}{J'_{21} H_{11} - J_{11} H'_{21} R^N_{P1} R^N_{F2}}\right)\\
&\to \frac{T^N_{F2}}{T^N_{P2}}\left(\frac{J'_{21} R^N_{P2} - H'_{21}}{J'_{21} - H'_{21} R^N_{F2}}\right).
\end{aligned} \tag{19}$$

Using Eqs. (19) and (7) and performing an expansion in terms of $k_{\mathrm{A}} R_C$, we recover the expansion (18) where the scattering part of the Green tensor of the resonator in the absence of the cavity, also in the limit $\epsilon_1 \to \infty$, is explicitly given by

$$\boldsymbol{G}_{\mathrm{B}}^{R}(\mathbf{r}_{\mathrm{A}},\mathbf{r}_{\mathrm{A}},\omega_{\mathrm{A}}) = -\frac{i\sqrt{\epsilon}k_A}{6\pi}\frac{H'_{21}}{J'_{21}}\boldsymbol{I} = -\frac{i\sqrt{\epsilon}k_A}{6\pi}\left(1+i\frac{Y'_{21}}{J'_{21}}\right)\boldsymbol{I}. \tag{20}$$

According to Eqs. (18) and (20) the density of states [Eq. (3)] can be decomposed into two parts:

$$\bar{A}(\omega) = \bar{A}_C(\omega) + \bar{A}_B(\omega), \tag{21}$$

$$\bar{A}_C(\omega) = \mathrm{Im}\left[\frac{3(\epsilon-1)}{2\epsilon+1}\frac{1}{(kR_{\mathrm{C}})^3} + \frac{9(\epsilon-1)(4\epsilon+1)}{5(2\epsilon+1)^2}\frac{1}{kR_{\mathrm{C}}}\right] = \frac{9\epsilon_I}{|2\epsilon+1|^2}\frac{1}{(kR_C)^3} + \frac{9(28|\epsilon|^2+16\epsilon_R+1)\epsilon_I}{5|2\epsilon+1|^4}\frac{1}{kR_{\mathrm{C}}}, \tag{22}$$

$$\bar{A}_B(\omega) = \mathrm{Im}\left[\frac{9\epsilon^{5/2}}{(2\epsilon+1)^2}\frac{Y'_{21}}{J'_{21}}\right]. \tag{23}$$

Here $\bar{A}_B(\omega)$ represents only the second term in $\boldsymbol{G}_{\mathrm{B}}^{R}$ [Eq. (20)]. The first, trivial term cancels out a similar contribution within the square brackets in the second line of Eq. (18). The dependence of the local-field effect on the medium density (manifested herewith via the magnitude of the cavity radius R_C) is exclusively represented by $\bar{A}_C$. This term shows that the strength of the local-field correction increases with increasing medium density, or reducing cavity radius, as can be expected on physical grounds. Another factor that may strongly affect the local-field correction is the strength of the medium-electromagnetic field interaction, characterized by the medium permittivity. The imaginary part of the permittivity is especially important in two respects. It determines at which rate the energy is irreversibly transferred from the guest atom to the neighboring medium constituents, thus no longer being available for the strong-coupling regime, and it determines at which rate the emitted photon is absorbed while propagating in the medium. Obviously the medium permittivity is present in both terms $\bar{A}_C$ and $\bar{A}_B$ in Eq. (21) for $\bar{A}$. As can be seen from Eq. (22), the first term $\bar{A}_C$ shows only a weak-frequency dependence, and can be expected to contribute to $\bar{A}$ in the form of a monotonous background. Meanwhile, the second term $\bar{A}_B$, which is associated with the Green tensor $\boldsymbol{G}_B^R$, is responsible for the position and width of the resonance lines; factors which are crucial for the strong-coupling regime [cf. Eqs. (2) and (4)]. Note that by restricting ourselves to the leading terms in the expansion (18), the dependence of the resonance line positions on the cavity radius R_C is lost. Assuming that

$$\epsilon_I \ll \epsilon_R, \tag{24}$$

a requirement that is usually fulfilled in practice, a resonance frequency ω_m can be found to satisfy [see Eq. (A14) in the Appendix]

$$\tan\bar{n}_R(\omega_m) = -\frac{\bar{n}_R(\omega_m)}{\bar{\epsilon}_R(\omega_m)-1}, \tag{25}$$

where

$$n = n_R + in_I = \sqrt{\epsilon(\omega_m)}, \quad \epsilon = \epsilon(\omega_m) = \epsilon_R + i\epsilon_I, \tag{26}$$

$$\bar{n} = n\frac{\omega_m}{c}R_w, \quad \bar{\epsilon} = \bar{n}^2, \tag{27}$$

and R_w is the radius of the mirror wall. Disregarding $\bar{A}_{\mathrm{C}}$, the resonance line at ω_m is of Lorentzian shape with peak values for the density of state [see the paragraph below Eq. (A14) in the Appendix],

$$\bar{A}_{\mathrm{B}}(\omega_m) \simeq \mathrm{Re}\left[\frac{9\epsilon^{5/2}}{(2\epsilon+1)^2}\right]\frac{\bar{\epsilon}_R^2-\bar{\epsilon}_R+1}{\bar{\epsilon}_R(\bar{\epsilon}_R-2)}\frac{1}{\bar{n}_I}, \tag{28}$$

and half width at half maximum

$$\delta\omega_m \simeq \bar{n}_I\frac{\bar{\epsilon}_R(\bar{\epsilon}_R-2)}{\bar{\epsilon}_R^2-\bar{\epsilon}_R+1}\frac{c}{n_R R_w}. \tag{29}$$

The above formulas show that the amplitude of the peak $\bar{A}_{\mathrm{B}}(\omega_m)$ is inversely proportional to n_I, while the half width at half maximum is proportional to n_I. Note that in the case of a normalized Lorentz distribution $f(x) = \frac{1}{\pi}\frac{\delta}{(x-x_0)^2+\delta^2}$, the peak value and the half width at half maximum are related via $f(x_0) = \frac{1}{\pi}\frac{1}{\delta}$.

The local-field correction effects inferred from Eqs. (18) and (20) are corroborated by the numerical results presented in Fig. 2, where the density of states $\bar{A}(\omega)$ [Eqs. (7) and (8)] as a function of frequency is plotted using the approximate formulas (18) and (20) for the Green tensor. Furthermore, the medium surrounding the guest atom is assumed to be of the Drude-Lorentz type with a single-resonance permittivity,

$$\epsilon(\omega) = 1 + \frac{\omega_{\mathrm{P}}^2}{\omega_{\mathrm{T}}^2-\omega^2-i\omega\gamma}, \tag{30}$$

where the plasma frequency ω_{P} characterizes the coupling strength between the medium polarization and the electromagnetic field, and ω_{T} and γ, respectively, are the position and the width of the medium resonance. Since the medium that fills the resonator will be kept more or less the same in the three models considered, all the frequencies and lengths, respectively, can be scaled with respect to ω_T and $\lambda_T = 2\pi c/\omega_T$. The imaginary part of the permittivity reads as $\epsilon_I(\omega) = \frac{\omega_{\mathrm{P}}^2\omega\gamma}{(\omega_{\mathrm{T}}^2-\omega^2)^2+\omega^2\gamma^2}$. If we are off resonance with respect to the medium absorption line and if γ is small, condition (24) is readily fulfilled. With the parameters chosen in Fig. 2, as ω varies from $0.3\omega_T$ to $0.6\omega_T$, the real and imaginary parts of $\epsilon(\omega)$ range from 5.4 to 7.25 and from 2.9×10^{-4} to 1.17×10^{-3}, respectively.

Figure 2 shows that the resonator supports multiple resonances. In Fig. 2(c) for example, the quality factor $Q = \omega_m/(2\delta\omega_m)$ decreases from 1.9×10^4 for the peak in the very left to 9.3×10^3 for the one in the very right. Note that in this idealized model of a perfect mirror, there is no output loss and the only source of line broadening is the material absorption. In Figs. 2(a) and2(b), together with the total $\bar{A}$, we have plotted $\bar{A}_C$ separately (lines marked by crosses), which reveals that the appearance of the plateau at the base of the peaks is predominantly due to the contribution from $\bar{A}_C$. For case (a) (the smallest chosen cavity radius $R_C = 0.001\lambda_T$) the contribution of the local-field correction $\bar{A}_C$ to $\bar{A}$ is considerable, a third or even more of the peak values, and the resonance lines clearly cannot be regarded as Lorentzian. Note that R_C cannot be set arbitrarily small because as R_C decreases at some point the macroscopic theory would cease to be valid. As the cavity radius increases [compare Figs. 2(a)–2(c)], the

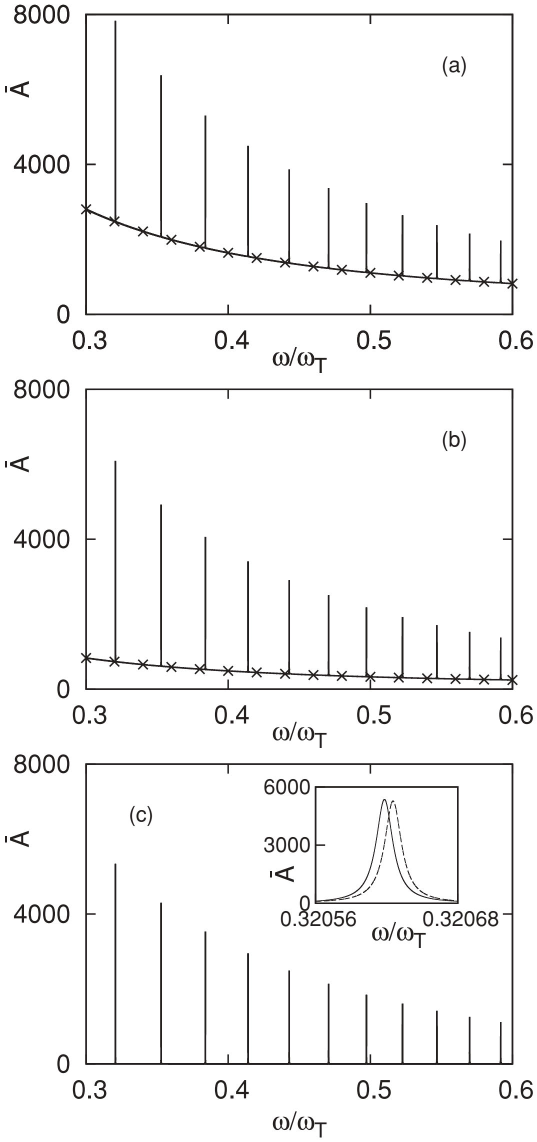

FIG. 2. The density of the field states $\bar{A}(\omega)$ of a perfect resonator having radius $R_w(=R_1)$ and filled by a Lorentz-type dielectric with permittivity (30). The parameters are $\omega_P = 2\omega_T$, $\gamma = 2\times 10^{-4}\omega_T$, $R_w = 6\lambda_T$ ($\lambda_T = 2\pi c/\omega_T$), and (a) $R_C = 0.001\lambda_T$, (b) $R_C = 0.0015\lambda_T$, and (c) $R_C = 0.01\lambda_T$. The lines marked by crosses in (a) and (b) are the contributions from $\bar{A}_C(\omega)$. The inset in (c) compares the approximate result (solid line) with the exact result (dashed line) for $R_C = 0.03\lambda_T$.

plateau level is gradually lowered and eventually becomes negligible.

In general, the numerical results as shown in Fig. 2 can be based on the the small-cavity approximation [Eq. (21) together with Eqs. (22) and (23)]. For same values of R_C and on the same scale as in the figure, the exact curves derived from the second line of Eq. (19) would be visually indistinguishable from the approximate ones. Clearly the approximation becomes less satisfying with increasing cavity radius. In the inset of Fig. 2 the exact curves are compared with the approximate ones for $R_C = 0.03\lambda_T$, where the peak near $\omega \simeq 0.32\omega_T$, meaning that $k_A R_C \simeq 0.06$, is considered. This is the peak to the very left in the main figure. The inset shows that the approximate (solid line) curve is shifted to the left and its amplitude is somewhat higher compared to the exact one. Numerical calculations show that the larger the resonance frequency is, the more pronounced these discrepancies become. The linewidths however remain roughly the same for the exact and the approximate curves, in consistency with the fact that the line broadening has its only source in the material absorption.

The behavior of the resonance linewidth, the Rabi frequency, and the ratio between them as functions of the cavity radius R_C are illustrated in Fig. 3 using the exact Eqs. (8) and (19). Different curves correspond to different degrees of material absorption. The curves begin at $R_C/\lambda_T = 0.0011$ for $\gamma/\omega_T = 10^{-4}$, $R_C/\lambda_T = 0.0015$ for $\gamma/\omega_T = 2\times 10^{-4}$ [cf. Fig. 2(b)], and $R_C/\lambda_T = 0.005$ for $\gamma/\omega_T = 10^{-3}$. These are values of R_C such that the plateau level of $\bar{A}(\omega)$ is about one tenth of its amplitude at the chosen resonance frequency. Since this plateau level gets lowered when R_C increases, the resonance line can be roughly regarded as being Lorentzian for all data presented in Fig. 3. Figure 3(a) shows that the linewidth normally increases with increasing material absorption, in accordance with $\delta\omega_m \sim n_I(\omega_m) \sim \epsilon_I(\omega_m) \sim \gamma$, which can be inferred from Eqs. (29), (A11), and (30). However in the region of small R_C at the beginning of each curve, one observes an increase of the linewidth as R_C decreases, which is obviously due to an enhancement of direct energy transfer from the guest atom to the closely located neighboring constituents of the medium. The decrease may become quite drastic as can be seen on the scale used in the inset in Fig. 3(a). When the medium becomes more absorbing, the region of drastic change moves toward higher values of R_C. For values of R_C below this region of drastic change (not shown), together with line broadening, the plateau level rises fast in proportion with $1/R_C^3$ [Eq. (22)] and it can be expected that the strong-coupling regime, if it exists, would quickly disappear. This is also manifested in the behavior of the ratio $\Omega/\delta\omega_m$ [Fig. 3(c)] discussed below. Beyond this region direct energy transfer is apparently no longer significant, and the linewidth is now determined by the gradual absorption that takes place when the emitted light propagates inside the medium enclosed within the resonator wall. As a consequence, $\delta\omega_m$ levels off and can be described reasonably well by the approximate equation (29). Note that the resonance line actually chirps slightly toward higher frequencies with increasing R_C [see Fig. 2(c), inset]. In particular at $R_C/\lambda_T = 0.0015, 0.03, 0.1$, ω_m/ω_T takes on the values of $0.3206\,1811$, $0.320\,625\,33$, $0.320\,862\,49$, respectively. For $\omega_m/\omega_T = 0.3206\,1811$ and the three values of γ in Fig. 3(a), Eq. (29) predicts $\delta\omega_m/\omega_T \simeq 4.67\times 10^{-6}$, 9.35×10^{-6}, and 4.67×10^{-5}, which is in good agreement with exact results represented by the solid, dashed, and dotted curves, respectively.

Assuming exact resonance $\omega_A = \omega_m$ between the guest atom and the medium-assisted electromagnetic resonator field, and choosing $A_0\lambda_T/(2c) = 10^{-6}$ as representative value of the atom-field coupling strength, in Fig. 3(b) we have plotted the R_C dependence of the Rabi frequency [Eq. (2)] for the same parameters as in Fig. 3(a). As the cavity radius R_C decreases, both $A(\omega_m)$ and $\delta(\omega_m)$ increase, resulting in an increase in Ω [cf. Eq. (2)]. Note that an increase in Ω does not necessarily imply the strong-coupling regime, since it is the ratio $\Omega/\delta\omega_m$,

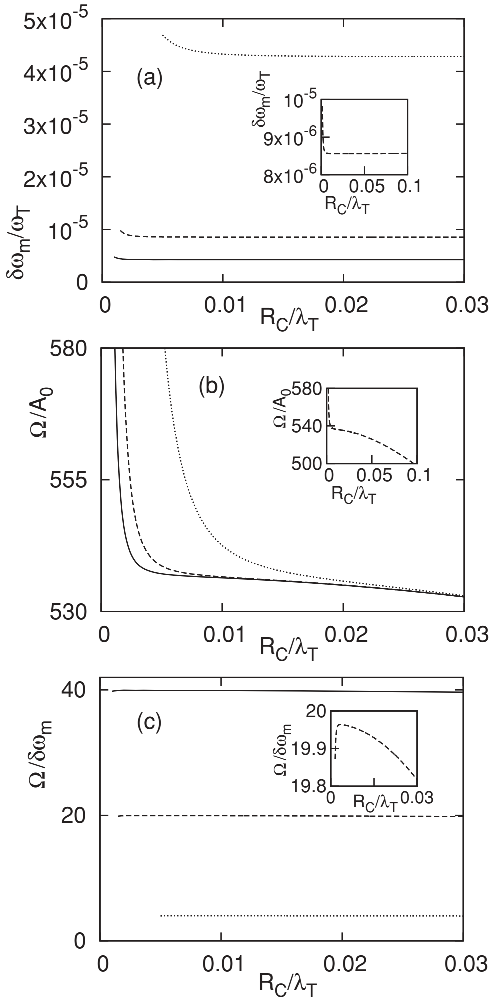

FIG. 3. (a) The half width at half maximum, (b) the Rabi frequency, and (c) the ratio between the two $\Omega/\delta\omega_m$ as functions of the cavity radius R_C/λ_T for different degrees of material absorption: $\gamma/\omega_T = 10^{-4}$ (solid line), 2×10^{-4} (dashed line), and 10^{-3} (dotted line). The insets present the behavior of the respective quantities on a larger scale for the middle case of $\gamma/\omega_T = 2\times10^{-4}$. The atom-field coupling strength is set at $A_0\lambda_T/(2c) = 10^{-6}$ and the resonance line at the very left of Fig. 2 is chosen. The remaining parameters are taken from Fig. 2.

not Ω alone, that can signal the onset of the strong-coupling regime. So the steep increase of Ω with decreasing R_C at the beginning of each curve is not indicative of the strong-coupling regime, since it originates from the enhanced nonradiative decay associated with the direct energy transfer to the medium. Around $R_C/\lambda_T \sim 0.03$, the curves for different values of γ merge into one, which can be explained as follows. For large enough R_C, the contribution of $\bar{A}_C$ to $\bar{A}$ becomes insignificant, $\bar{A} = \bar{A}_C + \bar{A}_B \simeq \bar{A}_B$ [see Eqs. (21)–(23) and Fig. 2]. Then using Eqs. (2), (28), and (29) we find

$$\frac{\Omega}{A_0} \to \sqrt{2\pi\bar{A}_B(\omega_m)\frac{\delta\omega_m}{\omega_T}\frac{2c}{A_0\lambda_T}} = \sqrt{\mathrm{Re}\left[\frac{9\epsilon^{5/2}}{(2\epsilon+1)^2}\right]\frac{\lambda_T}{n_R R_w}\frac{2c}{A_0\lambda_T}}, \qquad (31)$$

which, in leading order, does not depend on γ. Figure 3(b) and the inset also show that the curves do not converge to a constant value but keep going down. This trend is not covered by the approximate equation (31) above, which produces an almost constant $\Omega/A_0 \simeq 561$. Further numerical calculations show that the long-range reduction of the Rabi frequency is caused by an enlargement of the size of the real cavity. As the cavity radius increases, the cavity wall interferes with the constructive interferences that are the origin of the resonance lines, thereby lowering their heights. Clearly when the cavity radius approaches that of the mirror, then high-quality resonance lines reappear.

The approximate equations (28) and (29) can be also very helpful in predicting the occurrence of the strong-coupling regime. Indeed, using them in Eq. (4) yields

$$\frac{\Omega}{\delta\omega_m} \simeq \frac{\bar{\epsilon}_R^2-\bar{\epsilon}_R+1}{\bar{\epsilon}_R(\bar{\epsilon}_R-2)}\frac{1}{\pi n_I}\frac{\omega_T}{\omega_m}\sqrt{\mathrm{Re}\left[\frac{9\epsilon^{5/2}}{(2\epsilon+1)^2}\right]\frac{n_R\lambda_T}{R_w}\frac{A_0\lambda_T}{2c}}, \qquad (32)$$

which indicates that the strong-coupling regime is favored under the conditions of large atom-field electric dipole coupling strength, small material absorption, small resonance frequency, and small resonator size. Equation (32) yields $\Omega/\delta\omega_m \simeq 38.2, 19.1, 3.8$ for $\gamma/\omega_T = 10^{-4}, 2\times10^{-4}, 10^{-3}$, respectively, in good agreement with the exact numerical results presented in Fig. 3(c). However, it cannot describe the details of the curves including the sharp drop near the beginning [see Fig. 3(c), inset] and the subsequent downward going trend. Recall that we have not extended the curves towards values of R_C smaller than those in the figure for the reason that then the resonance lines can no longer be regarded as Lorentzians. If R_C is slightly reduced further, the nonradiative energy transfer to the medium would predominate the radiative emission process leading to an irreversible loss of the emitted photon. One can notice that all three curves gradually go down as R_C increases, which is consistent with the fact that the linewidth remains almost the same [see Fig. 3(a), inset], while the Rabi frequency decreases rather quickly [see Fig. 3(b), inset]. This phenomenon is clearly a consequence of the fact that, as already mentioned below Eq. (31), when the cavity size is sufficiently enlarged, then the cavity boundary starts to interfere destructively with the formation of the resonance lines. Since this is noticeable even at cavity sizes much smaller than the atomic transition wavelength, it can be regarded as a local-field correction.

IV. LORENTZ BAND-GAP MIRROR

In the previous section we have assumed the idealized situation where the resonator wall—the outermost, infinitely extended layer 1—is described by $\epsilon_1 \to \infty$, so that no light can leak from the resonator. Suppose now that the resonator wall is of finite thickness and has a Drude-Lorentz permittivity ϵ_w defined as in Eq. (30). In the spectral range between the transverse resonance frequency ω_{wT} and the longitudinal frequency $\omega_{wL} = \sqrt{\omega_{wT}^2 + \omega_{wP}^2}$, the permittivity exhibits a so-called Lorentz band gap, making the resonator wall well reflecting, while still allowing for a finite amount of output coupling. A similar resonator model is employed in Ref. [28] for a study of the strong-coupling regime in the absence of a medium surrounding the guest atom. The expansion in Eq. (18) again turns out to be quite helpful. Since the resonator now consists of four layers [Fig. 1(b)], the Green tensor $\boldsymbol{G}_B^R(\mathbf{r}_A,\mathbf{r}_A,\omega)$ is that of a three-layer geometry, which in the case of $r_A = 0$ reads as

$$\begin{aligned}
&\boldsymbol{G}_B^R(\mathbf{r}_A,\mathbf{r}_A,\omega)\\
&= \frac{i\omega}{6\pi c}\boldsymbol{I}\Big\{[k_3 H_{32} H'_{22} - k_2 H'_{32} H_{22}][k_2 J_{21} H'_{11} - k_1 J'_{21} H_{11}]\\
&- [k_2 H_{21} H'_{11} - k_1 H'_{21} H_{11}][k_3 H_{32} J'_{22} - k_2 H'_{32} J_{22}]\Big\}\\
&\times \Big\{[k_3 J_{32} H'_{22} - k_2 J'_{32} H_{22}][k_2 J_{21} H'_{11} - k_1 J'_{21} H_{11}]\\
&- [k_2 H_{21} H'_{11} - k_1 H'_{21} H_{11}][k_3 J_{32} J'_{22} - k_2 J'_{32} J_{22}]\Big\}^{-1}. \quad (33)
\end{aligned}$$

We are specifically interested in resonators large enough to feature at least one resonance line, that is, $R_w \frac{\omega}{c} = \frac{R_w}{\lambda} 2\pi \gtrsim 1$ [$R_w = R_2$ in the three-layer cavityless geometry described by the Green tensor (33)]. To simplify Eq. (33) in order to gain some insight analytically, we make the more stringent assumption that

$$R_w \frac{\omega}{c} \gg 1. \quad (34)$$

Within the band gap and away from the medium absorption line we have $\epsilon_{wR}(\omega) < 0$, $\epsilon_{wI}(\omega) > 0$, and $\epsilon_{wI}(\omega) \ll |\epsilon_{wR}(\omega)|$, resulting in $n_{wR}(\omega) \simeq \frac{\epsilon_{wI}(\omega)}{2\sqrt{|\epsilon_{wR}(\omega)|}}$, $n_{wI}(\omega) \simeq \sqrt{|\epsilon_{wR}(\omega)|} \sim 1$, and $n_{wR}(\omega) \ll n_{wI}(\omega)$. Recalling that $\epsilon_w(\omega) \equiv \epsilon_3(\omega)$ in a four-layer geometry which includes a cavity, but $\epsilon_w(\omega) \equiv \epsilon_2(\omega)$ in a three-layer cavityless geometry, it then follows that J_{21}, $J'_{21} \sim \exp(-ik_2 R_1)$. Taking into account that H_{il}, $H'_{il} \sim \exp(ik_i R_l)$ [see Eqs. (A3) and (A6) in the Appendix], and requiring that the resonator wall has a sufficiently high reflectivity,

$$e^{-n_{wI}(R_1 - R_2)\omega/c} \gg 1, \quad (35)$$

we may simplify Eq. (33) greatly, which together with Eqs. (3) and (6) again leads to Eqs. (21) and (22), but with $\bar{A}_B(\omega)$ being replaced by

$$\bar{A}_B(\omega) \simeq \mathrm{Im}\left[\frac{9\epsilon^{5/2}}{(2\epsilon+1)^2} \frac{k_3 Y_{32} H'_{22} - k_2 Y'_{32} H_{22}}{k_3 J_{32} H'_{22} - k_2 J'_{32} H_{22}}\right]. \quad (36)$$

The resonance frequencies ω_m of $\bar{A}_B(\omega)$ can be found to satisfy the equation [see the paragraph below Eq. (A19) in the Appendix]

$$\tan \bar{n}_R(\omega_m) = -\frac{n_R(\omega_m)}{n_{wI}(\omega_m)}, \quad (37)$$

where $\bar{n}_R$ is defined as in Eq. (27). Again, it can be shown that $\bar{A}_B(\omega)$ gives rise to resonance lines of Lorentzian shape with peak values [see the paragraph below Eq. (A19) in the Appendix]

$$\bar{A}_B(\omega_m) \simeq \mathrm{Re}\left[\frac{9\epsilon^{5/2}}{(2\epsilon+1)^2}\right] \frac{n_{wI}^2 + n_R^2}{\bar{n}_I(|n_w|^2 + |n|^2) + n_{wR} n_R} \quad (38)$$

and linewidths

$$\delta\omega_m = (\delta\omega_m)_1 + (\delta\omega_m)_2, \quad (39)$$

$$(\delta\omega_m)_1 \simeq \frac{|n_w|^2 + |n|^2}{n_{wI}^2 + n_R^2} \bar{n}_I \frac{c}{n_R R_w} \simeq \bar{n}_I \frac{c}{n_R R_w}, \quad (40)$$

$$(\delta\omega_m)_2 \simeq \frac{n_{wR}}{n_{wI}^2 + n_R^2} \frac{c}{R_w}. \quad (41)$$

Note that for an empty resonator ($n_R = 1, n_I = 0$), Eqs. (37)–(41) reproduce the results in Ref. [28]. On the other hand, if the absorption by the resonator wall is negligibly small, $\epsilon_{wI} \simeq 0$, then $(\delta\omega_m)_2 \simeq 0$, $\delta\omega_m \simeq (\delta\omega_m)_1 \simeq \bar{n}_I \frac{c}{n_R R_w}$, and the perfectly reflecting-wall result (29) is recovered [under condition (34) the coefficient $\frac{\bar{\epsilon}_R(\bar{\epsilon}_R - 2)}{\bar{\epsilon}_R^2 - \bar{\epsilon}_R + 1}$ tends to one].

The linewidth in Eq. (39) consists of two parts, where $(\delta\omega_m)_1$ is clearly attributable to the absorption by the medium enclosed within the resonator wall, and $(\delta\omega_m)_2$ is attributable to the absorption by the resonator wall itself. When a photon leaks from the resonator, it can either be captured by the cavity wall or can escape to the outer (empty) space. Due to the thick-resonator-wall assumption (35), the results (38)–(41) clearly can account for the first process only. Finally, the ratio between the Rabi frequency and the linewidth that determines whether the strong-coupling regime occurs reads as, in accordance with Eqs. (4) and (38)–(41),

$$\frac{\Omega}{\delta\omega_m} \simeq 2\frac{n_{wI}^2 + n_R^2}{\bar{n}_I(|n_w|^2 + |n|^2) + n_{wR} n_R} \times \sqrt{\mathrm{Re}\left[\frac{9\epsilon^{5/2}}{(2\epsilon+1)^2}\right] \frac{n_R R_w}{\lambda_T} \frac{A_0 \lambda_T}{2c}}. \quad (42)$$

In Fig. 4 the Rabi frequency/linewidth ratio as functions of γ_w and $R_1 - R_2$ is plotted, and the inset shows the density of states $\bar{A}(\omega)$ as a function of ω. The medium inside the resonator is the same as in Fig. 2. We have fixed the parameters of the resonator-wall permittivity in such a way that the Lorentz band gap covers the range from $\omega_{wT}/\omega_T = 0.3$ to $\omega_{wL}/\omega_T \simeq 0.35$. Hence only two peaks located within the gap survive (cf. Fig. 2), the remaining ones being absent because their frequencies are beyond the zone of high reflectivity. The positions of the two peaks do not coincide exactly with any one in Fig. 2 due to the difference in the geometry. For the value of the cavity radius used in Fig. 4, $R_C/\lambda_T = 0.005$ [larger than that in Fig. 2(b) but smaller than that in Fig. 2(c)] the plateau level is insignificant. Otherwise the two resonances fit well in to the pattern in Fig. 2 in the sense that the smaller the resonance frequency is, the higher its quality factor becomes. In Fig. 4(a) the resonator wall thickness is fixed at a large value such that the photon has very little chance of escaping to the outer space. The value of $\Omega/\delta\omega_m$ at $\gamma_w = 0$ is better than that in Fig. 3(b) (dashed line) because as we just mentioned the resonance line here has a higher Q factor. As the wall absorption increases, $\Omega/\delta\omega_m$ decreases. At about $\gamma_w/\omega_T \simeq 5.5 \times 10^{-5}$, the contribution from the wall material absorption $n_{wR} n_R$ to the denominator of $\Omega/\delta\omega_m$ [Eq. (42)] becomes equal to that from the material-inside-the-resonator absorption $\bar{n}_I(|n_w|^2 + |n|^2)$, and the ratio $\Omega/\delta\omega_m$ is reduced by a factor of 2. As γ_w/ω_T increases further to about 10^{-4}, the condition $\Omega/\delta\omega_m \gg 1$ is no longer satisfied, meaning that the weak-coupling regime takes over. In Fig. 4(a) we also plotted

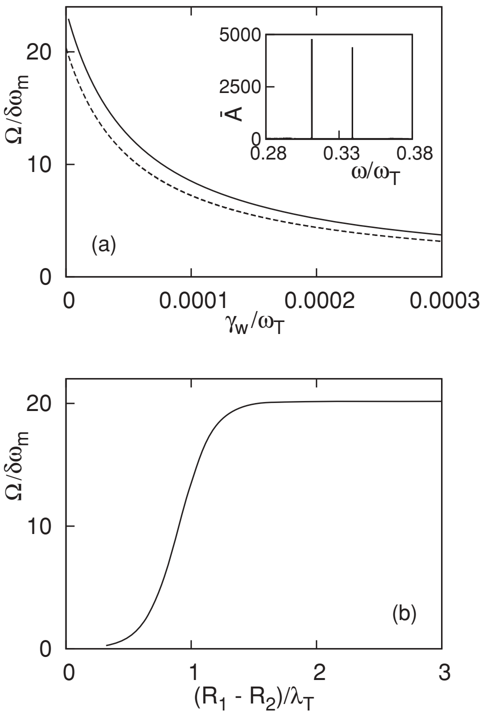

FIG. 4. The ratio $\Omega/\delta\omega_m$ for (a) the fixed resonator-wall thickness $(R_1-R_2)/\lambda_T=5$ and varying resonator-wall absorption and (b) the fixed resonator-wall absorption $\gamma_w/\omega_T=10^{-5}$ and varying resonator wall thickness. The medium that fills the resonator has a Drude-Lorentz type permittivity [Eq. (30)] with transverse frequency ω_T and $\omega_P/\omega_T=2, \gamma/\omega_T=2\times10^{-4}$. The resonator wall is described by the same kind of permittivity with $\omega_{wP}/\omega_T=0.3, \omega_{wP}/\omega_T=0.18$. Other parameters are the atom-field coupling strength $A_0\lambda_T/(2c)=10^{-6}$, the cavity radius $R_C\equiv R_3/\lambda_T=0.005$, the radius of the inner resonator wall $R_2/\lambda_T=6$, and the resonance frequency $\omega_m/\omega_T=0.311\,379\,14$. This resonance is the one on the left in the inset, which shows $\bar{A}(\omega)$ for the same parameters as above, and for $(R_1-R_2)/\lambda_T=5$ and $\gamma_w/\omega_T=10^{-5}$. The solid lines are obtained on using the exact Green tensor for a four-layer geometry, while the dashed line in (a) is obtained on using the approximate equation (42).

the approximate result (42) (dashed line) which shows a good qualitative agreement with the exact one. The discrepancy arises mainly from the error caused by Eqs. (39)–(41) for the linewidth.

Figure 4(b) shows an example of the dependence of the ratio $\Omega/\delta\omega_m$ on the thickness of the resonator wall. The degree of the wall absorption is kept at an insignificant value of $\gamma_w/\omega_T=10^{-5}$. Figure 4(b) shows that when the resonator wall is too thin, then light can leak easily to the space outside the wall and thus has a very little chance of being recaptured by the guest atom, that is, no strong coupling regime can be observed. Clearly, as the wall becomes thicker, light can be trapped better by the resonator, giving rise to the appearance of more and more distinct regions of the strong-coupling regime. Beyond a certain range of thicknesses, which is determined by the degree of material losses in the wall, an increase in the wall thickness no longer leads to an increase in $\Omega/\delta\omega_m$ because the electromagnetic field has only a finite penetration depth into the wall.

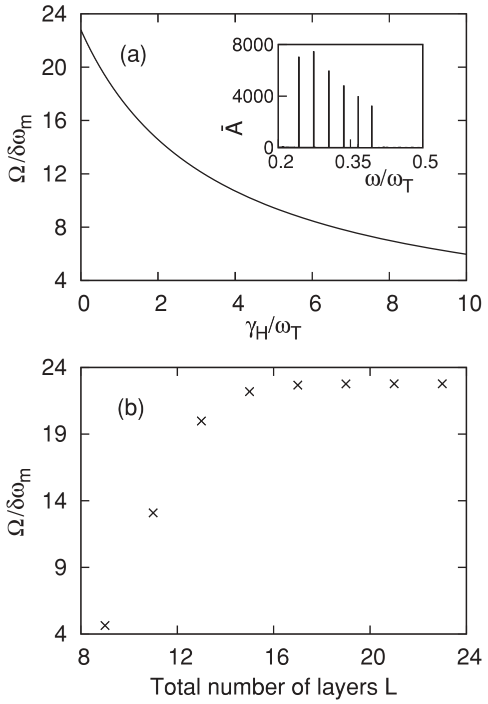

FIG. 5. (a) The ratio $\Omega/\delta\omega_m$ for the 23-layer configuration. The mirror consists of 20 layers having alternating low ε_L [defined as in Eq. (30) with $\omega_{LT}/\omega_T=20$, $\omega_{LP}/\omega_T=22.35\,78175$, $\gamma_L/\omega_T=10^{-3}$, i.e., $\varepsilon_L(\omega_0)=2.25+i\times10^{-6}$], and high permittivity ε_H [Eq. (30) with $\omega_{HT}/\omega_T=20$, $\omega_{HP}/\omega_T=67.0734523$]. The mirror absorption is varied by tuning γ_H. The inset shows $\bar{A}(\omega)$ for $\gamma_H/\omega_T=10^{-3}$. (b) The ratio $\Omega/\delta\omega_m$ for a fixed $\gamma_H/\omega_T=10^{-3}$ and varying (total) number L of layers in the system. The number of mirror layers is $(L-3)$. The resonance at $\omega_m/\omega_T=0.305\,089\,31$ is chosen in (a) while in (b) it shifts slightly from this value to $\omega_m/\omega_T=0.30508250$ when the number of layers decreases from 23 to 9. In both cases, the innermost layer of the mirror has permittivity ε_L. The medium that fills the resonator and other parameters are the same as in Fig. 4.

V. BRAGG-DISTRIBUTED MIRROR

We now proceed to consider a type of mirror that can serve as an example of an observation scheme for local-field effects in the strong-coupling regime, namely spherical Bragg-distributed mirrors. This type of mirror is extensively discussed in Refs. [20,21] and realized recently [23–25]. They consist of multiple layers having interchanging low and high permittivities [Fig. 1(c)] and quarter-wavelength optical thickness $d_j=\lambda_0/[4\mathrm{Re}\sqrt{\varepsilon_j(\omega_0)}]$ ($\lambda_0\equiv2\pi c/\omega_0$, ω_0 is the midgap frequency). In Fig. 5 we have chosen $\omega_0/\omega_T=0.32$, so that the gap is centered at roughly the same frequency as in the case of the Lorentz band-gap mirror in Fig. 4. The highly contrasting permittivity values $\varepsilon_L(\omega_0)\simeq2.25$ and $\varepsilon_H(\omega_0)\simeq12.25$ are chosen such that the system resembles the one materialized in Ref. [23], where periodic silicon dioxide (refractive index 1.5) and silicon cladding (refractive index 3.5) is employed.

The numerical results presented in Fig. 5 are obtained by using the exact formulas (6), (7), and (9)–(16) for the Green tensor. It can be seen from Fig. 5(a), inset, that in contrast to the case of a perfectly reflecting mirror [cf. Fig. 2], and similarly to the case of a Lorentz band-gap mirror [cf. Fig. 4(a), inset], only resonances within the band gap are supported. Note that there is no resonance at exactly the midgap frequency because of the spherical geometry, and because the resonator is medium filled. In Fig. 5(a) the ratio $\Omega/\delta\omega_m$ is plotted as a function of the material absorption in the mirror, which is tuned by varying γ_H. The number of layer pairs in the mirror is fixed at 10 (the Bragg onion resonator in Ref. [23] contains eight pairs of $\mathrm{Si}/\mathrm{SiO}_2$ layers). It is seen that the ratio decreases with increasing γ_H, and around $\gamma_H/\omega_T \simeq 4.5$ a transition from the strong-coupling regime to the weak-coupling regime occurs. This corresponds to $\varepsilon_H \simeq 12.25 + i0.04$ or $n_H = \sqrt{\varepsilon_H} \simeq 3.5 + i0.005\,79$, with the corresponding extinction coefficient being equal to $\kappa \simeq 0.001\,65$. In Fig. 5(b) the ratio $\Omega/\delta\omega_m$ is plotted as a function of the number of mirror layers. The degree of material absorption in the mirror is assumed to be low, $\gamma_H/\omega_T = \gamma_L/\omega_T = 10^{-3}$. For the range of mirror-layer numbers used in Fig. 5(b), photon radiated to the outer space dominates mirror material absorption as a mechanism of radiationless loss. When the mirror is too thin (data point with $L = 9$, i.e., three pairs of layers in the mirror), the emitted photon can escape easily from the resonator and no strong-coupling regime is found. For $L = 11$ and up, the field confinement is good enough to sustain the strong-coupling regime. The increase of the $(\Omega/\delta\omega_m)$ ratio is saturated near $L = 19$, so that eight pairs of layers is the minimum number in order to achieve the most pronounced strong-coupling regime for the parameters used in Fig. 5(b).

So far we have assumed that the guest atom is located in vacuum within the cavity. The question may arise as to what happens if we remove the cavity altogether, that is, if we neglect the local-field effects completely. Clearly we can do so only when the material absorption is negligible, since only then the imaginary part of the bulk Green tensor and together with it the field density of states [Eq. (3)] is well behaved. In Fig. 6 the density of the field states $\bar{A}(\omega)$ at a particular resonance is plotted for a resonator filled by a nonabsorbing material. The lower solid curve is for a cavityless resonator while the dashed, dotted, and dash-dotted curves are for the case where the cavity is present. Figure 6 shows that in the first case $\bar{A}(\omega)$ is generally smaller than in the other case. An argument is [as can be inferred from Eq. (18)] that one of the local-field effects, namely the factor $[3\varepsilon/(2\varepsilon+1)]^2$ in front of $\boldsymbol{G}_B^R(\mathbf{r}_A,\mathbf{r}_A,\omega)$ is absent. Indeed, by multiplying the data of the lower solid curve by the factor $[3\varepsilon/(2\varepsilon+1)]^2$ we obtain a new set of data (upper solid curve) which is comparable in values with the curves representing the case where a cavity is present. Another phenomenon that would be missing when the cavity is excluded is the resonance frequency shift which becomes apparent when comparing the upper solid curve (no cavity present) with the dashed curve (cavity present, with a radius of $R_C/\lambda_T = 0.001$). This shift increases with increasing cavity radius, as the dotted curve $(R_C/\lambda_T = 0.002)$ and the dash-dotted curve $(R_C/\lambda_T = 0.003)$ indicate. Note that this shift is also absent if one employs the approximate formulas (18) or (21)–(23) to take into account the local-field corrections [see the discussion on the inset of Fig. 2(c)].

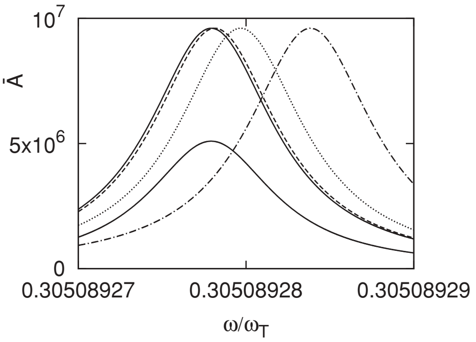

FIG. 6. The density of the field states $\bar{A}(\omega)$ at a particular resonance of a resonator filled by a nonabsorbing dielectric having the same Lorentz-type permittivity ε [Eq. (30)] as in Figs. 2–5, but with $\gamma = 0$. The two solid curves are for the case where the cavity is removed. The upper solid curve is the lower solid one multiplied by $[3\varepsilon/(2\varepsilon+1)]^2$. The remaining curves are for the cases where a cavity is included with radius $R_C/\lambda_T = 0.001$ (dashed line), 0.002 (dotted line), and 0.003 (dash-dotted line). Other parameters are the same as in Fig. 5.

VI. CONCLUSIONS

Within the real-cavity model we have investigated effects of local-field correction on the strong atom-field coupling regime by studying a system where the guest atom is positioned at the center of a spherical resonator. Three types of mirrors have been considered: a perfectly reflecting mirror, a Lorentz band-gap mirror, and a Bragg-distributed mirror. The first configuration establishes a deeper understanding of the local-field influence thanks to the simplicity of its Green tensor. The second one allows for a treatment of the influence of the output coupling, while the third one is an experimentally available system. We have used both the exact and an approximate formula of the Green tensor, the latter based on an expansion with respect to the smallness of the cavity size (as compared to the atomic transition wavelength), to gain insight into the effects of the local field.

We have shown that the local-field correction manifests itself in the form of a structureless background in the density of the field states. The level of this background is higher for higher material absorption and/or higher material density, with a net result that the resonance line is broadened and the strong-coupling regime may disappear. Although the approximate formula already reveals this effect, they cause an artificial shift in the frequency of the resonance line. By combining approximate analytical and exact numerical calculations, we have explored in detail the local-field effects on the Rabi frequency, the resonance line broadening, which also determines the exponentially decaying envelope of the vacuum Rabi oscillations, and the ratio between the two. In particular in the case of a Lorentz band-gap mirror, a too large resonator wall material absorption can destroy the strong-coupling regime. When the resonator wall is made thicker, it provides a better field confinement, thus facilitating the strong-coupling regime. However beyond some value of the wall thickness saturation is observed. This can be understood as resulting from the fact that the field has only a finite penetration depth into the resonator wall. Hence an increase in the resonator wall thickness beyond this depth does not provide additional field confinement.

The influence of the resonator wall on the strong-coupling regime can guide a design of an experimental setup, such as in the case with a Bragg-distributed mirror. For this configuration we have compared the case where the (real) cavity is left out altogether with the case where it is included, which can be done when the material absorption is negligible. We have found that the local-field correction leads to a resonance frequency shift, which increases with increasing cavity radius.

Finally, it should be pointed out that the local-field effects on the strong-coupling regime discussed here may be observed using Bragg onion resonators with, say, eight pairs of Si/SiO$_2$ of layers in the mirror [23]. This type of resonator can be created at the tip of an optical fiber. The strong-coupling regime can then be detected by looking out for the vacuum Rabi splitting in the spectrum of the emitted light channeled out of the resonator by way of a fiber.

ACKNOWLEDGMENTS

This research was supported by the Vietnam's National Foundation for Science and Technology Development (NAFOSTED) under Grant No. 103.99-2010.03. H.T.D. thanks the Alexander von Humboldt Stiftung for support.

LORENTZIAN SHAPE OF THE RESONANCE LINES

For an arbitrary position the Green tensor of a concentric multilayer sphere contains summations over spherical Bessel and Hankel functions of order n and their derivatives [22]. In the special case of an atom located at the center of the sphere, only spherical Bessel and Hankel functions of order one contribute. Here we need [29]

$$J_{il} = \frac{\cos z_{il}}{z_{il}^2}(\tan z_{il} - z_{il}), \tag{A1}$$

$$Y_{il} = -\frac{\cos z_{il}}{z_{il}^2}(1 + z_{il}\tan z_{il}), \tag{A2}$$

$$H_{il} = -\frac{e^{iz_{il}}}{z_{il}^2}(i + z_{il}), \tag{A3}$$

$$J'_{il} = \frac{\cos z_{il}}{z_{il}^3}\big(-\tan z_{il} + z_{il} + z_{il}^2\tan z_{il}\big), \tag{A4}$$

$$Y'_{il} = \frac{\cos z_{il}}{z_{il}^3}\big(1 + z_{il}\tan z_{il} - z_{il}^2\big), \tag{A5}$$

$$H'_{il} = \frac{e^{iz_{il}}}{z_{il}^3}\big(i + z_{il} - iz_{il}^2\big). \tag{A6}$$

We treat the case of a perfectly reflecting mirror and that of a Lorentz band-gap mirror separately.

Perfectly reflecting mirror

Using condition (24) we obtain from Eq. (23)

$$\bar{A}_{\mathrm{B}}(\omega) \simeq \mathrm{Re}\left[\frac{9\epsilon^{5/2}}{(2\epsilon+1)^2}\right]\mathrm{Im}\frac{Y'_{21}}{J'_{21}}. \tag{A7}$$

From Eqs. (A4) and (A5) it follows that

$$\frac{Y'_{21}}{J'_{21}} = \frac{1 - z_{21}^2 + z_{21}t}{z_{21} + \big(z_{21}^2 - 1\big)t}, \tag{A8}$$

where

$$z_{21} = n(\omega)\frac{\omega}{c}R_w, \tag{A9}$$

$$t = t_R + it_I = \tan\left[n(\omega)\frac{\omega}{c}R_w\right]. \tag{A10}$$

Under condition (24) we may write

$$n_I 2n_R + O\big(n_I^3\big) \simeq \epsilon_I, \quad n_R \simeq \sqrt{\epsilon_R} + O\big(n_I^2\big), \tag{A11}$$

$$t_R \simeq \tan\left(n_R\frac{\omega}{c}R_w\right) + O\big(\bar{n}_I^2\big), \quad t_I \simeq \bar{n}_I\big(1 + t_R^2\big) + O(\bar{n}_I^3). \tag{A12}$$

Using Eqs. (A8)–(A12) in Eq. (A7) we obtain

$$\begin{aligned}\bar{A}_{\mathrm{B}}(\omega) \simeq{}& \mathrm{Re}\left[\frac{9\epsilon^{5/2}}{(2\epsilon+1)^2}\right]\bar{n}_I\big(1 + t_R^2\big)\bar{\epsilon}_R(\bar{\epsilon}_R - 2)\\ &\times\Big([\bar{n}_R + (\bar{\epsilon}_R - 1)t_R]^2 + \bar{n}_I^2\big\{[1 + 2\bar{n}_R t_R\\ &+ (\bar{\epsilon}_R - 1)\big(1 + t_R^2\big)]^2 - 4\bar{n}_R[\bar{n}_R\\ &+ (\bar{\epsilon}_R - 1)t_R]\big(1 + t_R^2\big)\big\}\Big)^{-1},\end{aligned} \tag{A13}$$

where terms proportional to $\bar{n}_I^3$ are dropped. The resonance lines ω_m of the resonator can be found by determining the complex roots of the denominator in Eq. (19) or, approximately, the denominator in Eq. (20). Then the real parts of the complex roots yield the line positions while the imaginary parts yield the corresponding linewidths. Here we employ another method, namely the condition $\frac{d\bar{A}_{\mathrm{B}}}{d\omega}\big|_{\omega=\omega_m} = 0$, which allows us to also easily figure out the line shape. For simplicity we leave out the term proportional to $\bar{n}_I^2$ in the denominator while calculating $\frac{d\bar{A}_{\mathrm{B}}}{d\omega}$. As a function of ω, ϵ typically varies slowly compared with t_R, and $\frac{d\epsilon}{d\omega}$ can be neglected. The afore mentioned condition then yields

$$t_R(\omega_m) = -\frac{\bar{n}_R(\omega_m)}{\bar{\epsilon}_R(\omega_m) - 1} + O\big(\bar{n}_I^2(\omega_m)\big) \tag{A14}$$

and the peak value (28). Making an expansion of $t_R(\omega)$ around ω_m in the denominator of Eq. (A13) and keeping only terms up to the second order in $(\omega - \omega_m)$, it can be shown that the first-order term vanishes and the resonance lines have a Lorentzian shape with the half width at half maximum (29).

Lorentz band-gap mirror

Under condition (24) we can approximately write $\bar{A}_B$ [Eq. (36)] as

$$\bar{A}_B(\omega) \simeq \mathrm{Re}\left[\frac{9\epsilon^{5/2}}{(2\epsilon+1)^2}\right]\mathrm{Im}\left(\frac{k_3Y_{32}H'_{22} - k_2Y'_{32}H_{22}}{k_3J_{32}H'_{22} - k_2J'_{32}H_{22}}\right). \tag{A15}$$

Using $|z_{22}|^2 \gg 1$, $|z_{32}|^2 \gg 1$, which are more relaxed than the assumption (34), in Eqs. (A4)–(A6), we derive

$$J'_{32} \simeq \frac{\cos z_{32}}{z_{32}^2}(1 + z_{32}t), \tag{A16}$$

$$Y'_{32} \simeq \frac{\cos z_{32}}{z_{32}^2}(t - z_{32}), \tag{A17}$$

$$H'_{22} \simeq -i\frac{e^{iz_{22}}}{z_{22}^2}(i+z_{22}), \tag{A18}$$

where t is the same as in Eq. (A10). Substitution of these and Eqs. (A1)–(A3) in Eq. (A15) yields

$$\begin{aligned}\bar{A}_B(\omega) &\simeq \mathrm{Re}\left[\frac{9\epsilon^{5/2}}{(2\epsilon+1)^2}\right]\mathrm{Im}\left[\frac{ik_3(1+z_{32}t)+k_2(t-z_{32})}{-ik_3(t-z_{32})+k_2(1+z_{32}t)}\right]\\ &\simeq \mathrm{Re}\left[\frac{9\epsilon^{5/2}}{(2\epsilon+1)^2}\right]\mathrm{Re}\left(\frac{n_w-int}{n-in_wt}\right)\\ &\simeq \mathrm{Re}\left[\frac{9\epsilon^{5/2}}{(2\epsilon+1)^2}\right][\bar{n}_I(|n_w|^2+|n|^2)+n_{wR}n_R]\big(1+t_R^2\big)\\ &\quad\times\{(n_R+n_{wI}t_R)^2+[(n_I-n_{wR}t_R+n_{wI}t_I)^2\\ &\quad+2(n_R+n_{wI}t_R)n_{wR}t_I]\}^{-1},\end{aligned} \tag{A19}$$

where in going from the first line to the second one we make use of the relationships $|z_{22}| \gg 1$ and $|k_3z_{32}| \gg |k_2|$, which are consequences of Eq. (34). In contrast to the perfectly reflecting mirror model, here there are two small parameters $n_I \ll 1$ and $n_{wR} \ll 1$, and products of three or more of these small parameters are dropped in going from the second line to the third one. We also use Eq. (A12) and neglect n_In_{wI}, which is much smaller than $\bar{n}_I(|n_w|^2+|n|^2)$, due to Eq. (34). Now we can again apply the condition $\frac{d\bar{A}_B}{d\omega}\big|_{\omega=\omega_m}=0$ to search for the resonance frequencies. In doing so, the term in the square brackets in the denominator, which is quadratic in terms of small parameters, is neglected. The result is given in Eq. (37), which in turn produces a Lorentzian line shape with associated heights and widths given by Eqs. (38) and (39), respectively.

[1] H. A. Lorentz, Wiedem. Ann. **9**, 641 (1880).

[2] L. Onsager, J. Am. Chem. Soc. **58**, 1486 (1936).

[3] J. Knoester and S. Mukamel, Phys. Rev. A **40**, 7065 (1989).

[4] P. de Vries and A. Lagendijk, Phys. Rev. Lett. **81**, 1381 (1998).

[5] G. Juzeliunas, Phys. Rev. A **55**, R4015 (1997).

[6] M. Fleischhauer, Phys. Rev. A **60**, 2534 (1999).

[7] M. E. Crenshaw and C. M. Bowden, Phys. Rev. Lett. **85**, 1851 (2000); Phys. Rev. A **63**, 013801 (2000).

[8] P. R. Berman and P. W. Milonni, Phys. Rev. Lett. **92**, 053601 (2004) H. Fu and P. R. Berman, Phys. Rev. A **72**, 022104 (2005).

[9] S. Scheel, L. Knöll, D.-G. Welsch, and S. M. Barnett, Phys. Rev. A **60**, 1590 (1999).

[10] R. J. Glauber and M. Lewenstein, Phys. Rev. A **43**, 467 (1991).

[11] S. Scheel, L. Knöll, and D.-G. Welsch, Phys. Rev. A **60**, 4094 (1999).

[12] M. S. Tomaš, Phys. Rev. A **63**, 053811 (2001).

[13] A. Rahmani and G. W. Bryant, Phys. Rev. A **65**, 033817 (2002).

[14] Ho Trung Dung, S. Y. Buhmann, L. Knöll, D.-G. Welsch, S. Scheel, and J. Kästel, Phys. Rev. A **68**, 043816 (2003).

[15] G. L. J. A. Rikken and Y. A. R. R. Kessener, Phys. Rev. Lett. **74**, 880 (1995).

[16] P. Lavallard, M. Rosenbauer, and T. Gacoin, Phys. Rev. A **54**, 5450 (1996).

[17] F. J. P. Schuurmans, D. T. N. de Lang, G. H. Wegdam, R. Sprik, and A. Lagendijk, Phys. Rev. Lett. **80**, 5077 (1998).

[18] G. M. Kumar, D. N. Rao, and G. S. Agarwal, Phys. Rev. Lett. **91**, 203903 (2003).

[19] Ho Trung Dung, S. Y. Buhmann, and D.-G. Welsch, Phys. Rev. A **74**, 023803 (2006).

[20] T. A. Nguyen and Ho Trung Dung, Phys. Rev. A **76**, 033831 (2007).

[21] G. Burlak, *The Classical and Quantum Dynamics of the Multispherical Nanostructures* (Imperial College Press, London, 2004).

[22] L. W. Li, P. S. Kooi, M. S. Leong, and T. S. Yeo, IEEE Trans. Microwave Theory Tech. **42**, 2302 (1994).

[23] Y. Xu, W. Liang, A. Yariv, J. G. Fleming, and S.-Y. Lin, Opt. Lett. **29**, 424 (2004).

[24] I. Gourevich, L. M. Field, Z. Wei, C. Pachet, A. Petukhova, A. Alteheld, E. Kumacheva, J. J. Saarinen, and J. E. Sipe, Macromolecules **39**, 1449 (2006).

[25] R. Takekoh, W.-H. Li, N. A. D. Burke, and H. D. H. Stöver, J. Am. Chem. Soc. **128**, 240 (2006).

[26] Ho Trung Dung, L. Knöll, and D.-G. Welsch, Phys. Rev. A **57**, 3931 (1998).

[27] L. Knöll, S. Scheel, and D.-G. Welsch, in *Coherence and Statistics of Photons and Atoms*, edited by J. Peřina (John Wiley & Son, New York, 2001), p. 1.

[28] Ho Trung Dung, L. Knöll, and D.-G. Welsch, Phys. Rev. A **62**, 053804 (2000).

[29] *Handbook of Mathematical Functions*, edited by M. Abramowitz and I. A. Stegun (Dover, New York, 1973).